Electronic Supplementary Material (ESI) for Lab on a Chip.

Supplementary Information
Three dimensional tracking of nanoparticles by dual-color position retrieval in double-core microstructured optical fiber

Shiqi Jiang[ab], Ronny Förster[a], Adrian Lorenz[a], and Markus A. Schmidt[* abc]

[a]*Leibniz Institute of Photonic Technology, 07745, Jena, Germany*
[b]*Abbe Ceter of Photonics and Faculty of Physica, FSU Jena, 07745 Jena, Germany*
[c]*Otto Schott Institute of Material Research, FSU Jena, 07745 Jena, Germany*

S.1 Fabrication of double core microstructured optical fiber

The fiber fabrication approach used here relies on the stack-and-draw technique. An MCVD manufactured Germanium doped preform was grinded and polished to match the required core-to-clad diameter ratio and drawn to two different diameters. These elements acting as cores are stacked together with additional undoped silica rods of different diameters into a silica tube. This preform was drawn and sintered to an intermediate diameter in a cane drawing step. This cane was then inserted into another silica tube forming the final preform which was then drawn down to fiber. Online pressurization allows for the adjustment of the fiber geometry while drawing.

S.2 The finite element simulations of fiber modes

The modal simulations were carried out by using the 'Electromagnetic Waves' module from COMSOL Multiphysics within the wavelength range 635 nm $< \lambda <$ 670 nm. The refractive index of the cladding (ncladding) was calculated using the definition of the Sellmeier Equation given in ref. [1]. The refractive index of two cores (n_{core}) was slightly higher than the cladding, which is estimated to be $n_{core} = n_{cladding} + 7.5 \cdot 10^{-3}$. The value for the refractive index increase has been chosen such to reach single mode operation at the operating wavelength. The refractive index of water was determined according to ref.[2]. Note that to spatially resolve the electromagnetic field patterns sufficiently, a very fine mesh inside the microchannel has been used (maximum element extension 3 nm).

S.3 Experimental setup for dual-color 3D tracking

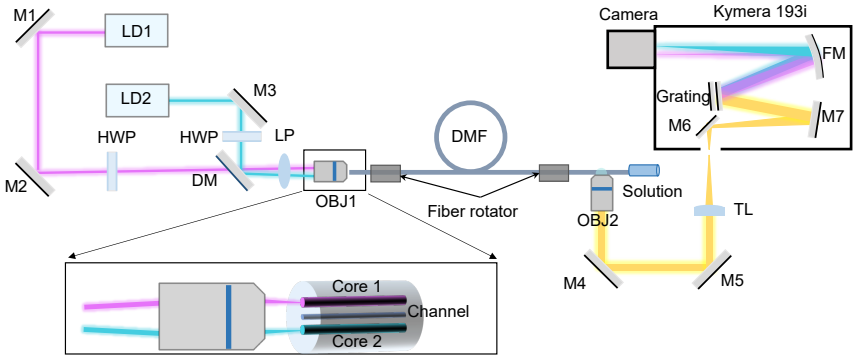

Figure S1 Sketch of the experimental setup for 3D tracking of nanoparticle based on double core microstructured fiber (details can be found in the text below).

Light from two laser diodes (LD1 and LD2) with different wavelengths (λ = 663 nm and λ = 647 nm) are coupled into the double core microstructured fiber (DMF) through a 40x objective (OBJ1). A dichroic mirror (DM) was used to split the two beams which allows the two beams to be focused at different positions (into two cores), separately. To control the relative orientation of the input beam polarization, connection line of the cores/microchannel and the microscope objective (OBJ 2), two fiber rotators are used at both ends of the fiber. Half waveplates (HWP) and a linear polarizer (LP) are used to control the polarization of the input beams. The input beam polarization is tuned to be perpendicular to the connection line between two cores for stronger scattered intensity from nanoparticles in order to collect more scattered light considering the dipole oscillation. The particle solution is filled from the fiber output end via capillary force. The fiber is immersed in refractive index matching oil (n $\sim$ 1.456) within the observation region and the scattered light from the particles is collected by a 60x oil immersed objective (OBJ2). This light is then focused by a tube lens (TL) into the entrance of the spectrograph (Andor Kymera 193i). The beams of different wavelengths are separated by a grating (150I/mm) and focused onto different regions of the camera by a focusing mirror (FM).

S.4 Imaging quality

The excellent imaging properties of our approach are exemplarily demonstrated by the raw image shown in Figure S2. To make the relevant features more visible, the image contrast has been increased (normalization with 0.3% pixel saturation). Clearly visible are the first Airy rings, which show aberration-free imaging and thus reveal a very high recording quality. Based on this observation, the influence of the circular microchannel on the imaging and thus on the tracking procedure can be safely neglected.

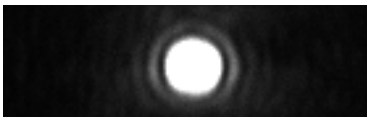

Figure S2 Example of one frame of the diffusing gold nanosphere with strongly enhanced image contrast to make the relevant imaging features more visible (image has been cropped image).

S.5 Verification of correlation between intensity and y-position by simulation

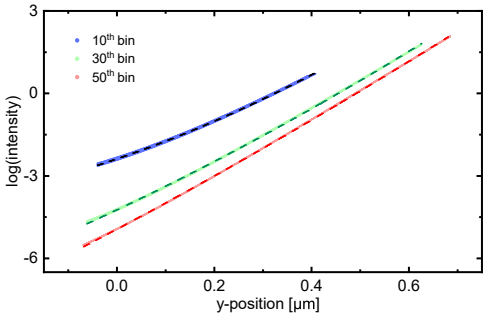

Figure S3 Dependencies of the intensity (in logarithmic scale) on y-positions (dashed lines) and corresponding second-order polynomial fits (solid lines) in the 10^{th} (purple), 30^{th} (green) and 50^{th} (red) bin.

By using the simulation procedure described in S2, we obtain the field distribution in the microchannel as shown in the manuscript (Figure 2 (f), (g)). For each mode, we divide the field intensity according to their x-positions into different bins and analyze the correlation function between the field intensity and the y-position bin-by-bin. Here we used 100 bins in total across the entire channel in a similar way to the evaluation of the experimental data. Considering the geometric symmetry along the center line of the mcirochannel (x = 0) of the fiber, which leads to a symmetric field distribution in the channel, we combine the intensity in x-symmetric bins into one bin, finally forming 50 bins in total. For each bin, we use in the following the combinations of intensity/y-position which belong to the higher intensity half down to 55% of the highest intensity (e.g., if the intensity varies from 0 to 1 with y-positions from 0 to 1, then we take the intensity/y-positions within the y-range from 0.45 to 1). The correlation between the

intensity and y-positions in that region is well described by an exponential function $I = e^{a(x)\cdot y^2+b(x)\cdot y+c(x)}$ in each bin. As examples, the intensity vs. y-position dependencies for the 10^{th}, 30^{th} and 50^{th} bin for one of the two modes are plotted in Figure S3.

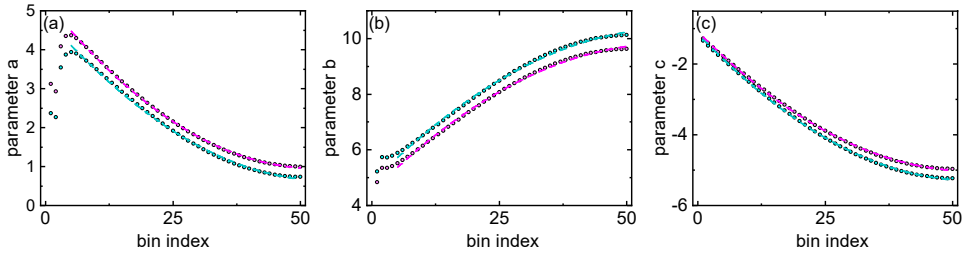

Figure S4 Dependencies of the fitting parameters for the exponential function that describes the functional dependence between intensity and y-positions ($I = e^{a(x)\cdot y^2+b(x)\cdot y+c(x)}$) obtained from simulations (magenta: 663 nm in larger core; cyan: 647 nm in smaller core). Dots: simulated data. Dashed lines: second polynomial fitting ($a(x) = p_1\cdot x^2+p_2\cdot x+p_3$) from the 6th bin to the last bin (a) parameter a. (b) parameter b. (c) parameter c.

By applying the exponential fitting function bin-by-bin, we obtain the fitting parameters in each bin as shown in Figure S4 for the example of the 663 nm in the bigger core (magenta circles) and 647 nm in the smaller core (cyan circles). Note that the dependency of the fitting parameters on the x-position is also be well described by second-order-polynomial functions (e.g., $a(x) = p_1 \cdot x^2 + p_2 \cdot x + p_3$) as indicated by the dashed curves in Figure S4. Here, we excluded the points from the first 5 bins due to the numerical artifacts emerging in the simulation.

S.6 Calibration of x and z positions between 2 colors

Theoretically, the locations of a single particle obtained from two colors should be identical. However, due to the dispersion induced by the grating, the scattering images from two colors are located on different zones in the camera as indicated in Figure S5 (a), demanding a calibration for the offset of x-positions between two colors. First, we calculate the difference for all dual-color x-positions $\Delta x = x^{dc}_{663nm} - x^{dc}_{647nm}$, where x^{dc}_{663nm} and x^{dc}_{647nm} represent the x-positions in each dual-color frame (Figure S5 (b)). Then we shift the x-positions for one color with respect to the mean of the Δx between two colors such that the offset of the x-difference for calibrated positions is zero:

$$x^{cal}_{647nm} = x_{647nm} + mean(\Delta x) \tag{1}$$

Here, x^{cal}_{647nm} and x_{647nm} represent the calibrated and originally measured x-positions belonging to the 647 nm set. We performed this calibration procedure for the z-positions as well to remove the offset of the slight difference in z-positions between the two colors, which is supposed to come from the slight inclination between the camera and the spectrograph (Andor's Kymera 193i).

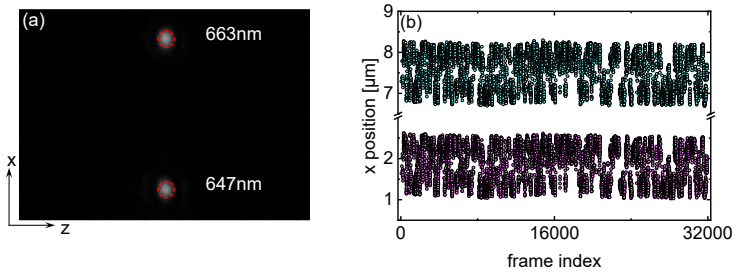

Figure S5 (a). Raw image of one frame which demonstrates the separation of images between the two colors (top: 663 nm, bottom: 647 nm). (b). Plot of original x-positions solely for the dual-color frames for two colors.

S.7 Correction of the inclination of fiber

In the experiment, the fiber might be placed at a slight angle on the lens, creating an inclination between the z-direction recorded by the camera and the expected z-direction (direction of fiber axis). Thus, a

correction to compensate for this inclination is required. Given a sufficiently long enough observation time and enough sampling, we could assume the diffusive particle reached the maximum allowed displacement in the channel cross-section, i.e., roughly the diameter of the channel. The dynamic range of x-position ($dx = x_{max} - x_{min}$) in case of perfect fiber alignment parallel to the camera (z-direction) $dx^{parallel}$ (Figure S6 (a)) should always be smaller than that in the case of fiber being placed with an inclination dx^{tilt} (Figure S6 (b)). Therefore, we performed a correction by assuming different inclination angles and compare the corresponding dx. In case of the inclination correction with the correct angle, the value of dx should be lower than those of incorrect angles. Therefore, we determine the correct inclination angle by finding the minimum of $dx = dx(\theta)$. With the known inclination angle, the corrected positions are calculated as follows:

$$x_{correction} = x_{raw} \cdot \cos(\theta) - z_{raw} \cdot \sin(\theta) \tag{2}$$

$$z_{correction} = z_{raw} \cdot \cos(\theta) + x_{raw} \cdot \sin(\theta) \tag{3}$$

The raw and corrected x-z positions are shown in Figs. S6 (c) and (d), respectively.

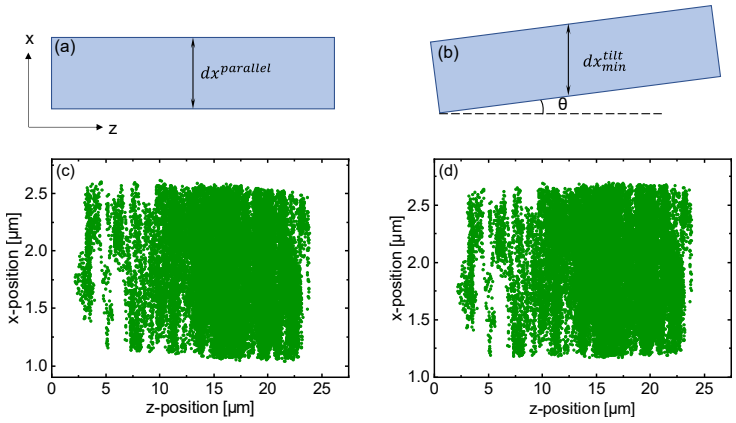

Figure S6 Sketches of fiber being placed (a) parallel to the camera z-direction and (b) with an inclination angle θ. (c) x- and z-positions originally obtained from camera images without inclination correction. (d). Corresponding positions after the inclination correction.

S.8 Selection of intensity-position sets

We pick up several sets of y-position/intensity in each bin for the exponential function determination. Specifically speaking, in each bin, we suppose that the brightest scattering (I_1, 100% percentile rank of the intensity) from one mode appears at the y-position closest to the corresponding core, namely y_1 and the median scattering ($I_{1/2}$, 50% percentile rank of intensity) appears at the middle y-position, namely $y_{1/2}$ in the bin. Similar to this, we could also select other position-intensity sets, for instance at another two y-positions (e.g., $y_{5/6}$ and $y_{2/3}$ in Figure S7) where each half bin is trisected between y_1 and $y_{1/2}$ with the corresponding intensity values at the trisected-y-position estimated from simulations. Then together with the [y_1, I_1] and [$y_{1/2}$, $I_{1/2}$] sets, we could fit the resulting data points with the exponential function defined by Eq. (1) and obtain the three parameters $a(x)$, $b(x)$ and $c(x)$ bin-by-bin. Here, the criteria of determining the intensity for a certain y-position is to choose the intensity with the same percentile rank as that for the trajectory which is at that y-position. For example, if we want to know the corresponding intensity at $y_{5/6}$ (illustrated in Figure S7), we could count the percentage of the number of trajectories which is below $y_{5/6}$, namely $P_{5/6}$, and we select the intensity with the percentile rank of $P_{5/6}$. In a homogeneously distributed trajectory case, the percentage of the trajectory number within a certain y-position range in a bin is equal to the percentage of the y-position range among the whole y-position range, leading to the value $P_{5/6}$ being 5/6. Note that in this case, the trajectory percentage is not equal to the percentage of y-positon range any more due to the inhomogeneous distribution of trajectory in the channel originating from the confinement. Specifically, the local viscosity of the fluid in the channel at different radial position r along the transverse dirction (fiber cross section) is modified by the resistance coefficient $R_t(\Lambda, r)$ [3] [4], leading to different viscosity $\eta(r)$ at different radial positions. The gradually decreasing diffusion rate with closer proximity to the wall leads to longer sojourn time and therefore

denser distribution of trajectory with the proximity to the wall. As a result, the distribution of the particle trajectory in the channel is expected to rely on the radial-position-dependent resistance coefficient. To obtain the correct percentile rank of intensity at the defined y-positions as described above, we perform 1000 hindered Brownian motion simulations along the transverse dimensions, each having a length of 32000 frames (same as in the experiment), in which each random walk step $\Delta x/\Delta y$ follows a modified norm distribution:

$$Norm(\mu = 0, \sigma = \sqrt{\frac{2D_0 t}{R_t(\Lambda, r)}})$$

Here,$R_t(\Lambda, r)$ is the resistant coefficient (details in S11) at radial position r within the fiber cross-section, Λ is the size ratio between nanoparticle and channel, and t is the time interval of 1/1388.9 s (same as in experiment) between two steps in simulation. The free diffusion rate is given by $D_0 = \frac{k_b T}{6\pi\eta_0 r_n p}$ (k_b: Boltzmann constant, T = 25 °C: temperature, η_0= 0.89 cP: viscosity, r_{np} = 43 nm: nanoparticle radius). In the simulation, the channel diameter is taken to be 1500 nm in correspondence with the measured cross-section of the microchannel (SEM picture in Figure 2b). We analyzed the distribution of the simulated trajectories and estimated the intensity percentile rank of intensity/trajectory corresponding to certain y-positions. Here the percentile rank indicates the percentage of trajectories which are located below the corresponding y-position as well as the percentage of intensity which is weaker than the intensity at the corresponding y-position. We select two y-positions which trisect the y_1 and $y_{1/2}$ in a certain bin, namely, $y_{5/6}$ and $y_{2/3}$ as illustrated in Figure S7 (a) and calculate the average percentile rank value with the error bar of standard deviation in each bin among 1000 simulations (Figure S7 (b)). Note that the amount number of bins is taken to be the same as for the experimental data, thus dividing trajectories into 100 equal bins along the x-direction and combining the symmetric bins, overall forming 50 bins. Guided by the simulation, in experimental data analysis, for the 1^{st} to 9^{th} bin, we take the percentile ranks respectively which gradually varies from 92.4% to 81.2% for $y_{5/6}$ and from 74.1% to 64.9% for $y_{2/3}$ For the remaining bins, we take the averaged percentile ranks from 10th bin to 50th bins, which are 80.2% and 64.8% for $y_{5/6}$ and $y_{2/3}$, respectively.

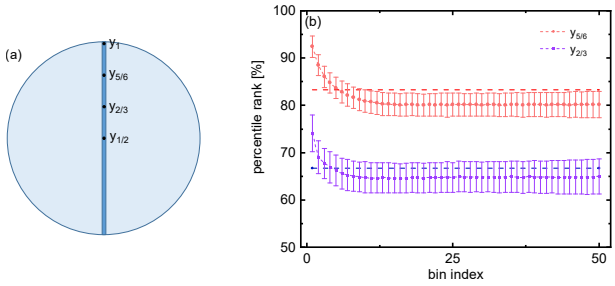

Figure S7 (a). Sketch illustrating the selection of y-positions in the microchannel for obtaining the intensity/position combinations required for the fitting. In each bin, y_1 and $y_{1/2}$ represent the y-position which is closest to the corresponding core and the median y-positions (corresponding to the highest intensity and the median intensity). Additionally, $y_{5/6}$ and $y_{2/3}$ represent the y-positions which trisect the half bin region betweeny_1 and $y_{1/2}$. (b) The corresponding averaged percentile rank with error bar (standard deviation) of intensity/trajectory at $y_{5/6}$(red) and $y_{2/3}$ (purple), respectively, obtained from 1000 hindered Brownian motion simulations. The red and purple dashed lines mark the expected percentile rank for non-hindered (homogeneously distributed trajectory) case.

S.9 Prevention of empty frames

It is important that the x-position and the scattered intensity for each wavelength is known for every frame, as otherwise the estimation of percentile rank would be biased. To prevent the impact of empty frames which occasionally appear due to invalid tracking in case of low scattering intensity, the missing positions are obtained from the other wavelength and corresponding scattered intensity is set to zero. This is a valid procedure as although the nano-object can disappear in some frames for one wavelength, it can always be located within the image of the other wavelength. Compared to the trackable frames, the scattered intensity for the empty frames should be much lower. So, if we assume the intensity value for the empty frames, which are mostly in the darker half-range, to be zero, with the percentile rank determinations, which only apply to the brighter half region, not being affected.

S.10 Intensity ratio threshold for filtering out intensity from ambiguous regions

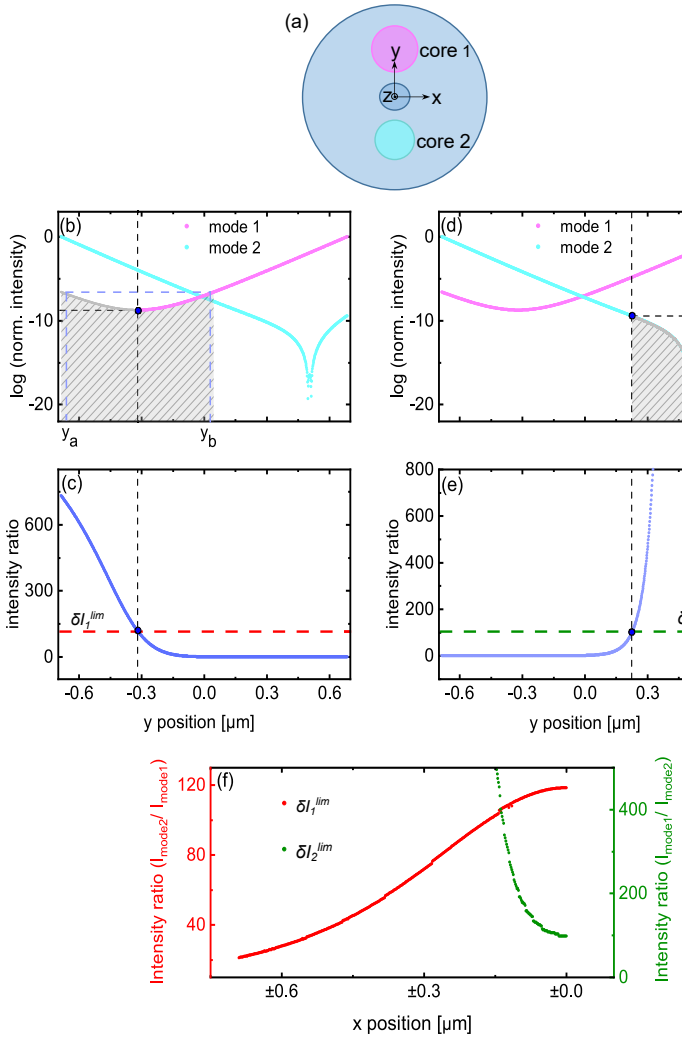

Figure S8 (a) Sketch of the DMF with coordinates system. (b) Logarithm of normalized intensity as a function of the y-position in the center of the structure (x = 0) for two modes (mode 1 (magenta): large core, λ= 663 nm; mode 2 (cyan): small core, λ = 647 nm). The grey curve indicates the y-positions of mode 1 which belong to the ambiguous region (with grey and dashed background) and should be excluded from the intensity-mediated position retrieval. The boundary between the retrievable and non-retrievable y-positions is marked by the vertical black dashed line located at the y-position with the lowest intensity. (c) Corresponding intensity ratio between mode 2 and mode 1 δI_1. The red dashed line marks the intensity ratio limit δI_1^{lim}. The black dashed line represents the same as in (b). (d) Similar plot to (b), now concentrating on the ambiguous region of mode 2. The boundary between the retrievable and non-retrievable y positions is marked by the vertical black dashed line, which is located at the y-position with the lowest unique intensity value. (e). Corresponding intensity ratio. The green dashed line marks the appropriate intensity ratio limit δI_2^{lim}. (f) The intensity ratio limit dependence on x-positions for two modes.

As we explained in the text, there are ambiguous spatial regions for each mode where one intensity value corresponds to multiple y-positions in certain bins. Therefore, we need to pick up the intensity which belongs to the non-ambiguous region, i.e, 55 percent of y-position area with relative higher intensity in each bin, for position retrieval. However, by relying on the relative intensity from one mode, we are not able to distinguish which region the intensity belongs to: For example, in the case of mode 1 (Figure S8 (b)), the intensity value for the positions y_a and y_b are the same, which in turn means that we cannot decide if the nano-object is within the retrievable region. However, an unambiguous assignment can be realized through including the intensity value from the other mode: even though the intensity for mode 1 at y_a and y_b are identical (magenta and grey curves in Figure S8 (b)), the corresponding intensity value of the other mode (cyan curve) is very different. Therefore, we introduce the intensity ratio between the

two values at the same y-position ($\delta I_1 = I^{norm}_{mode,2}/I^{norm}_{mode,1}$ and $\delta I_2 = I^{norm}_{mode,1}/I^{norm}_{mode,2}$) as an assignment indicator that unambiguous correlates y-position and intensity in the respective spatial domains (Figure S8 (c)). For mode 1, all the frames with $\delta I_1 > \delta I_1^{limit}$ could be excluded from the position retrieval. Here δI_1^{limit} is defined as the ratio at the y-position at which the intensity of mode 1 is smallest (blue dot in Figure S8 (b)). Similarly, an intensity ratio limit can be determined for the other mode δI_2^{limit} (Figure S8 (d) and (e)) which specifically is defined here as the ratio at which the y-position/intensity correlation is unique. Therefore all the frames with intensity ratio above that limit are filtered out. Such an intensity ratio limit can be found for each x-position for each of the two modes (Figure S8 (f)). In experimental data analysis, we compare the normalized intensities from two colors for the dual-color frames and set the lower intensity to 0 once the intensity ratio between two colors is higher than an intensity ratio threshold in order to exclude invalid frames. To simplify the filtering process, we take a uniform intensity ratio for all x-positions (e.g., $\delta I_{1,2}^{limit} = 5$), which is lower than the minimum ratio value about 20 for two modes, thus creating a safety margin that takes into account the experimental uncertainties.

S.11 Resistance factor correction

As we mentioned in S8, due to the confinement of the microchannel, the local viscosity of the fluid in the channel at different radial position r is modified by the resistance coefficient $R_q(\Lambda, r)$ [3] leading to $\eta = \eta_0 \cdot R_q(\Lambda, r)$. Here is the size ratio between the particle diameter and the channel extension, η_0 is the bulk viscosity and $q = x, y, z$ denotes the different spatial direction [3]. According to ref. [3], the resistance coefficient by:

$$R_q(\Lambda, r) = \sum_{i=0}^{7} c_i^q(\Lambda) \cdot \Psi_i^q(\Lambda, r) \tag{4}$$

with the coefficient c_i^q and the expression Ψ_i^q, both of which can be found in the ref. [3].

In experiments, we calculate the hydrodynamic diameter of the particle by assuming the viscosity of the solution to be the bulk value, which leads to a biased determination of the particle size. Therefore, to obtain the correct hydrodynamic radius of the particle along the three spatial directions $r_q^{correct}(q = x, y, z)$ which in fact is estimated from the trajectories across the whole channel, we calculate the average resistance factor R_{avg} which could be used to describe the average of this resistance effect: $r_q^{correct} = r_q^{MSD}/R_q^{avg}$, with r_q^{MSD} being the radius we calculated directly from the MSD analysis. Mathematically, the average inverse resistance factor is defined via the cross-section integral of the inverse resistance function $R(\Lambda, r)$ (A: area of channel cross section, w: weight).

$$\frac{1}{R_q^{avg}} = \int\limits_{area} \left(\frac{1}{R(\Lambda, x, y)} w \cdot dA\right) \Big/ \int\limits_{area} w \cdot dA \tag{5}$$

The situation of having a cylindrical channel requires a transformation from Cartesian to polar coordinates ($dxdy = rdrd\phi$), leading to:

$$\frac{1}{R_q^{avg}} = \frac{\int_0^{2\pi} \int_0^{a-r_{np}} \frac{w}{R(\Lambda,r,\phi)} r \cdot drd\phi}{\int_0^{2\pi} \int_0^{a-r_{np}} wr \cdot drd\phi} = \frac{\int_0^{a-r_{np}} \frac{w}{R(\Lambda,r,\phi)} r \cdot dr}{\int_0^{a-r_{np}} wr \cdot dr} \tag{6}$$

Here the product of weight w and radius r should be the relative probability of the particle being at radial position r. Due to this resistance effect, the density of the particle trajectory in the channel is expected to be radial position dependent rather than to be homogeneous. To determine the function for the trajectory distribution, we perform hindered Brownian motion simulations in the transverse 2D dimension as described in S8 showing that the position density depends linearly on $R(\Lambda, r)$. This in turn means that the closer the particle is to the wall, the larger the resistance factor and the higher the probability that the particle will be located near the wall. Specifically, we perform a 2D hindered Brownian motion simulation for a 86nm-diameter particle in a 1500nm-diameter channel with 1 million steps and count the positions in each angular bin of width Δr ($\Delta r = 1nm$) (transparent region in Figure S9 (a)). As plotted in Figure S9 (b), the counts of the trajectories, which is proportional to the relative probability of the particle being there, are linearly correlated to the average of the product of the radial coordinate r and the resistance coefficient $R(\Lambda, r)$ which is given by $< r \cdot R(\Lambda, r) >$. As we mentioned before, the relative probability of the particle being at radial positionr is taken as the product of radial

position r and the weight w. Considering this, we choose the resistance function itself as a weight function ($w = R(\Lambda, r)$), making particle positions closer to the wall more relevant. So the average resistance factor can then be calculated as follows:

$$\frac{1}{R_q^{avg}} = \frac{\int_0^{a-r_{np}} r \cdot dr}{\int_0^{a-r_{np}} R(\Lambda, r) r \cdot dr} \tag{7}$$

Note that the expression of $R_q(\Lambda, r)$ given in Ref. [3] is not using Cartesian coordinates as we used in our work. The transformation of $R_q(\Lambda, r)$ to Cartesian coordinates has been discussed in ref. [4]

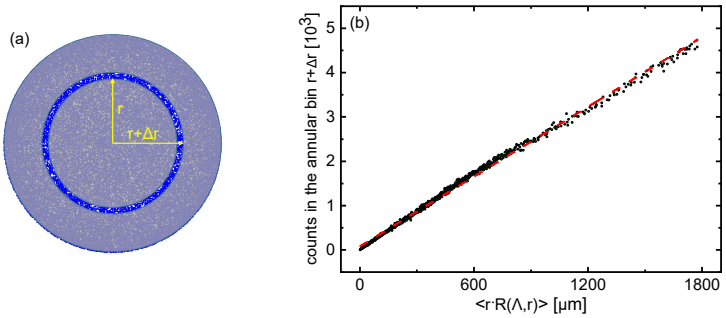

Figure S9 (a) Schematic of the simulated position distribution (blue dots) and the annular bin $r + \Delta r$ of width Δr (transparent region). (b) Dependency of the position count in the annular bin of width $\Delta r = 1nm$ on the averaged product of radial coordinate r and resistance coefficient $R(\Lambda, r)$. Green circles represent the count value. The red dashed line shows a linear fit to the points.

References

[1] Ian H Malitson. Interspecimen comparison of the refractive index of fused silica. *Josa*, 55(10):1205–1209, 1965.

[2] David J Segelstein. *The complex refractive index of water*. PhD thesis, University of Missouri–Kansas City, 1981.

[3] JJL Higdon and GP Muldowney. Resistance functions for spherical particles, droplets and bubbles in cylindrical tubes. *Journal of Fluid Mechanics*, 298:193–210, 1995.

[4] Shiqi Jiang, Ronny Förster, Malte Plidschun, Jens Kobelke, Ron Fatobene Ando, and Markus A Schmidt. Three-dimensional spatiotemporal tracking of nano-objects diffusing in water-filled optofluidic microstructured fiber. *Nanophotonics*, 9(15):4545–4554, 2020.